

Hyperon mixing and universal many-body repulsion in neutron stars

Y. Yamamoto,¹ T. Furumoto,² N. Yasutake,³ and Th. A. Rijken^{1,4}

¹*Nishina Center for Accelerator-Based Science, Institute for Physical and Chemical Research (RIKEN), Wako, Saitama 351-0198, Japan*

²*National Institute of Technology, Ichinoseki College, Ichinoseki, Iwate 021-8511, Japan*

³*Department of Physics, Chiba Institute of Technology, 2-1-1 Shibazono Narashino, Chiba 275-0023, Japan*

⁴*IMAPP, University of Nijmegen, Nijmegen, The Netherlands*

(Received 9 June 2014; revised manuscript received 1 September 2014; published 30 October 2014)

A multi-Pomeron exchange potential (MPP) is proposed as a model for the universal many-body repulsion in baryonic systems on the basis of the extended soft core (ESC) baryon-baryon interaction. The strength of the MPP is determined by analyzing the nucleus-nucleus scattering with the G -matrix folding model. The interaction in ΛN channels is shown to reproduce well the experimental Λ binding energies. The equation of state (EoS) in neutron matter with hyperon mixing is obtained including the MPP contribution, and mass-radius relations of neutron stars are derived. It is shown that the maximum mass can be larger than the observed one, $2M_{\odot}$, even in the case of including hyperon mixing on the basis of model parameters determined by terrestrial experiments.

DOI: [10.1103/PhysRevC.90.045805](https://doi.org/10.1103/PhysRevC.90.045805)

PACS number(s): 21.65.Cd, 21.80.+a, 25.70.-z, 26.60.Kp

I. INTRODUCTION

It is a fundamental problem to understand properties of baryonic many-body systems such as nuclei, hypernuclei, and neutron stars on the basis of underlying baryon-baryon (BB) interactions. The basic property of nuclear systems composed of nucleons is the saturation property of density and energy per particle. Though important roles for this property are played by repulsive cores and tensor components included in nucleon-nucleon (NN) interactions, it is insufficient quantitatively: We need to take into account the three-nucleon interaction composed of the attractive part (TNA) and the repulsive part (TNR). While the TNA contributes moderately as function of density, the TNR contribution increases rapidly in the high-density region and leads to high values of the nuclear incompressibility. It is well known that the latter is indispensable for the stiff equation of state (EoS) of neutron-star matter needed to reproduce large maximum masses of neutron stars.

The neutron stars J1614-2230 [1] and J0348-0432 [2] have brought great impacts on the maximum-mass problem, observed masses of which are $(1.97 \pm 0.04)M_{\odot}$ and $(2.01 \pm 0.04)M_{\odot}$, respectively. These large masses give a severe condition for the stiffness of the EoS of neutron-star matter, suggesting the existence of strong TNR.

On the other hand, the hyperon (Y) mixing in neutron-star matter is known to bring about the remarkable softening of the EoS, which cancels the TNR effect for the maximum mass [3–5]. One of the ideas to avoid this serious problem is to consider that the TNR-like repulsions work universally for YNN , YYN , YYY , as well as for NNN [5]. In this work we adopt this idea: Universal repulsions among three baryons are called here the three-baryon repulsion (TBR). The main subject in this paper is to investigate whether or not the maximum mass of $2M_{\odot}$ can be obtained from the EoS for hyperon-mixed neutron-star matter, when TBR is taken into account.

In order to treat hyperon-mixed nuclear matter realistically, it is indispensable to use a reliable interaction model for baryon-baryon (BB) channels including not only NN but also YN and YY : We adopt here the extended soft core (ESC) model developed by two of authors (T.R. and Y.Y.) and Nagels

[6]. In this model two-meson and meson-pair exchanges are taken into account explicitly and no effective boson is included differently from the usual one-boson exchange models. The latest version of ESC model is named ESC08c [6,7]. Hereafter, ESC means this version. The TBR is taken into account by the multi-Pomeron exchange potential (MPP) within the ESC modeling.

Some many-body theory is needed to treat many-body systems with a realistic BB interaction model: The G -matrix theory is a good tool for such a purpose, where the correlations induced by short-range and tensor components are renormalized into G -matrix interactions. Similarly baryonic coupling terms such as ΛN - ΣN ones are included this way into single-channel G matrices such as ΛN - ΛN ones. In the case of nucleon matter, the lowest-order G -matrix calculations with the continuous (CON) choice for intermediate single-particle potentials were shown to simulate well the results including higher hole-line contributions up to about 4 times normal density ρ_0 [8]. On the basis of this recognition, we study properties of baryonic matter including not only nucleons but also hyperons with use of the lowest-order G -matrix theory with the CON choice.

The methodology in our works is to use the BB interaction model determined on the basis of terrestrial experiments, namely to introduce no *ad hoc* parameter to stiffen the EoS. The most important is how to determine the strength of the TNR, which is an essential quantity for the stiffness of EoS. Many attempts have been made to extract some information on the incompressibility K of high-density matter formed in high-energy central heavy-ion collisions. In many cases, however, the results for the EoS still remain inconclusive. On the other hand, it was shown clearly in Ref. [9] that the TNR effect appeared in angular distributions of $^{16}\text{O} + ^{16}\text{O}$ elastic scattering ($E/A = 70$ MeV), etc. Such a scattering phenomenon can be analyzed quite successfully with the complex G -matrix folding potentials derived from free-space NN interactions. Then, the G -matrix folding potentials including MPP contributions are used to analyze the $^{16}\text{O} + ^{16}\text{O}$ scattering, and the strengths of MPP are adjusted so as to reproduce the experimental data.

The determined MPP interactions are included in constructing the EoS of neutron-star matter, and they are expected to result in an EoS stiff enough to give the observed neutron-star mass [10]. It should be noted that our MPP is defined so as to work universally not only in NNN states but also YNN , YYN , and YYY states. Corresponding to the determined MPP, the TNA is added phenomenologically to reproduce the nuclear saturation property precisely.

Thus, our BB interaction is composed of ESC, MPP, and TNA. ESC gives potentials in $S = -1$ (ΛN , ΣN) and $S = -2$ (ΞN , $\Lambda\Lambda$, and $\Lambda\Sigma$) channels. MPP is universal in these channels. Because TNA is given in NN channels phenomenologically, there is no theoretical correspondence in $S < 0$ channels. However, we can confirm the validity of the ESC + MPP + TNA model in these channels by applying this interaction to hypernuclear calculations, and then TNA is considered a three-baryon attraction (TBA).

The final step in this work is to study properties of neutron stars with hyperon mixing on the basis of our BB interaction model. The EoS of β -stable neutron-star matter composed of neutrons (n), protons (p^+), electrons (e^-), muons (μ^-), and hyperons (Λ and Σ^-) is derived from the G -matrix calculation with use of the ESC + MPP + TBA model. Using the EoS of hyperonic neutron-star matter, we solve the Tolmann-Oppenheimer-Volkoff (TOV) equation for the hydrostatic structure, and obtain mass-radius relations of neutron stars.

For a massive neutron star including hyperons, there are works based on the relativistic mean field models [11–13]. In comparison with these works, the feature of our approach is to start from the well-established BB interaction model, and to use no adjustable parameter except those in the additional many-body interactions determined in terrestrial experiments.

This paper is organized as follows: In Sec. II, BB interaction models are introduced. It is explained how to determine MPP and TBA parts. In Sec. III, the ESC + MPP + TBA model is tested by comparing the calculated result for Λ hypernuclei to experimental data. In Sec. IV, we derive the EoS of hyperonic nuclear matter. By solving the TOV equation, the mass-radius relations are obtained. The conclusion of this paper is given in Sec. V.

II. INTERACTION MODEL

A. Baryon-baryon interaction ESC

In Nijmegen ESC potentials, all available NN , YN , and YY , data are fitted simultaneously with single sets of meson parameters. In the most recently developed ESC-model (ESC08c) the dynamics consists of the following ingredients:

- (i) OBE potentials from pseudoscalar ($J^{PC} = 0^{-+}$), vector ($J^{PC} = 1^{--}$), scalar ($J^{PC} = 0^{++}$), and axial vector ($J^{PC} = 1^{+-}$) are treated with the most general vertices. Besides these, also included are the axial-vector mesons with $J^{PC} = 1^{+-}$. Two-meson-exchange (TME) potentials in ESC are restricted to two-pseudoscalar-exchange (ps-ps) potentials, where the full pseudoscalar nonets are exchanged.

- (ii) Meson-pair exchange (MPE). The two-meson-baryon-baryon vertices are the low-energy approximations of (a) the heavy mesons and their two-meson decays, and (b) contributions from baryon-resonance Δ_{33} , etc., and negative-energy states. The MPE interactions have been extended to all $\{8\} \otimes \{8\}$ BB channels by using $SU_f(3)$ symmetry. For example the Tomozawa-Weinberg pair-interaction potential is included in ESC.
- (iii) Diffractive contributions to the soft-core potential. The pomeron is thought of as being related to an even number of gluon-exchanges. Next to the Pomeron exchange (even number of gluons) also odderon exchange (odd number of gluons) is included in the OBE part of the interactions. Also, room is made for quark-core effects supplying extra repulsion, which may be required in some BB channels such as $\Sigma^+ p (I = 3/2, {}^3S_1)$ and $\Sigma N (I = 1/2, {}^1S_0)$ channels. We describe this structural effect phenomenologically by Gaussian repulsions, similar to the Pomeron. In ESC the strength of this repulsion is taken to be proportional to the weights of the $SU(6)$ -forbidden [51] configuration in the various BB -channels.

As a model of universal TBR, we introduce the multi-Pomeron exchange potential (MPP) [6], consistently with the ESC modeling, assuming that the dominant mechanism is triple and quartic Pomeron exchange.

The three- and four-body local potentials are derived from the triple- and quartic-Pomeron vertexes. The density (ρ) dependent two-body potentials in a baryonic medium are obtained by integrating over coordinates of third (and fourth) particles in the three-body (and four-body) potentials as follows:

$$V_{\text{eff}}^{(3)}(r) = g_p^{(3)}(g_p)^3 \frac{\rho}{\mathcal{M}^5} F(r), \quad (1)$$

$$V_{\text{eff}}^{(4)}(r) = g_p^{(4)}(g_p)^4 \frac{\rho^2}{\mathcal{M}^8} F(r), \quad (2)$$

$$F(r) = \frac{1}{4\pi} \frac{4}{\sqrt{\pi}} \left(\frac{m_p}{\sqrt{2}} \right)^3 \exp\left(-\frac{1}{2}m_p^2 r^2\right). \quad (3)$$

Here, the values of the two-body Pomeron strength g_p and the Pomeron mass m_p are the same as those in ESC. A scale mass \mathcal{M} is taken as a proton mass.

As stated in Ref. [10], values of $g_p^{(3)}$ and $g_p^{(4)}$ are roughly estimated from the experimental cross sections of the process $pp \rightarrow pX$ (diffractive production of showers of particles) at very high energies [14,15]: $g_p^{(3)}/g_p = 0.15$ – 0.20 and $g_p^{(4)} = 33$ – 228 .

B. Determination of MPP strength

In the same way as [10], the analyses for the ${}^{16}\text{O} + {}^{16}\text{O}$ elastic scattering at an incident energy per nucleon $E_{in}/A = 70$ MeV are performed so that the MPP strengths $g_p^{(3)}$ and $g_p^{(4)}$ are determined to reproduce the experimental data with the use of the G -matrix folding potential derived from ESC including MPP.

Because the nuclear saturation property cannot be reproduced only by adding MPP to ESC, we introduce also an attractive part phenomenologically as a density-dependent two-body interaction

$$V_A(r; \rho) = V_0 \exp[-(r/2.0)^2] \rho \exp(-\eta\rho) (1 + P_r)/2, \quad (4)$$

P_r being a space-exchange operator. Here, because the functional form is not determined within our analysis, it is fixed to be similar to the TNA part given in [16]. V_0 and η are treated as adjustable parameters. $V_A(r; \rho)$ works only in even states due to a $(1 + P_r)$ factor. This assumption is needed to reproduce the $^{16}\text{O} + ^{16}\text{O}$ potential at $E/A = 70$ MeV and nuclear-matter energy consistently [10].

Though there exist meson-theoretical models for TNA, our simple model in Eq. (4) enough to study properties of high-density EoS. Its strength is adjusted to reproduce the nuclear saturation property accurately. Then, this TNA part is not important for the stiffness of EoS in the high-density region, which is determined essentially by MPP.

On the basis of G -matrix calculations, strengths of the MPP part ($g_p^{(3)}$ and $g_p^{(4)}$) and the attractive part (V_0 and η) are determined so as to reproduce the $^{16}\text{O} + ^{16}\text{O}$ angular distribution at $E_{in}/A = 70$ MeV, and to reproduce the saturation properties of nucleon matter. The determined parameters are listed in Table I. Here, it should be noted that the ratio of $g_p^{(3)}$ and $g_p^{(4)}$ cannot be determined in our analysis. In the same way as Ref. [10], we choose it rather adequately by referring to the estimation given in [14,15]. Then, chosen values of $g_p^{(3)}$ and $g_p^{(4)}$ are included in set (a). On the other hand, $g_p^{(4)} = 0$ is taken in sets (b) and (c). Set (b) is determined to reproduce $^{16}\text{O} + ^{16}\text{O}$ angular distribution as well as set (a). Set (c) has the same value of $g_p^{(3)}$ as set (a). Hereafter, interactions ESC + MPP + TNA with sets (a), (b), and (c) are named MPa, MPb, and MPc, respectively.

The basic properties of nucleon matter are given by the following quantities: Denoting an energy per particle as $E(\rho, \beta)$ with $\beta = (\rho_n - \rho_p)/\rho$, a symmetric energy E_{sym} and its slope parameter L are expressed as $E_{\text{sym}} = \frac{1}{2} [\frac{\partial^2 E(\rho, \beta)}{\partial \beta^2}]_{\rho_0}$ and $L = 3\rho_0 [\frac{\partial E_{\text{sym}}(\rho)}{\partial \rho}]_{\rho_0}$, respectively. An incompressibility of symmetric nucleon matter is given by $K = 9\rho_0^2 [\frac{\partial^2 E(\rho, 0)}{\partial \rho^2}]_{\rho_0}$.

The E/A values for MPa/b (MPc) are -15.8 (-15.5) MeV at the saturation density $\rho_0 = 0.16 \text{ fm}^{-3}$. The values of E_{sym} at ρ_0 are 33.1, 33.1, and 32.7 MeV in the cases of MPa, MPb, and MPc, respectively, and the values of L are 70, 69, and 67 MeV correspondingly. These values are in nice agreement with the values $E_{\text{sym}} = 32.5 \pm 0.5$ MeV and $L = 70 \pm 15$ MeV determined recently on the basis of experimental data [17]. The obtained values of K at ρ_0 are 310, 280, and 260 MeV for

TABLE I. Parameter values included in MPP and TNA.

	$g_p^{(3)}$	$g_p^{(4)}$	V_0	η
(a)	2.34	30.0	-32.8	3.5
(b)	2.94	0.0	-45.0	5.4
(c)	2.34	0.0	-43.0	7.3

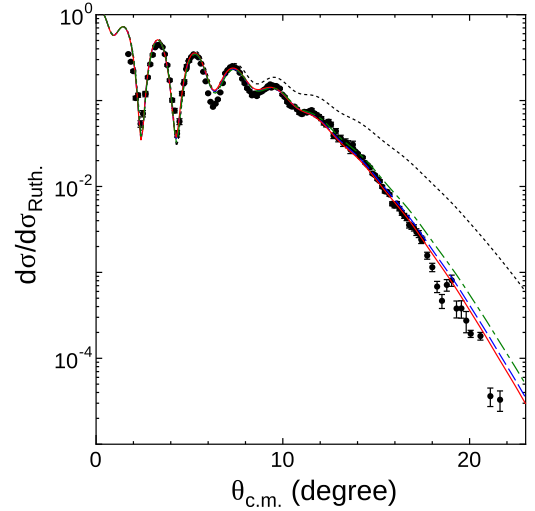


FIG. 1. (Color online) Differential cross sections for $^{16}\text{O} + ^{16}\text{O}$ elastic scattering at $E/A = 70$ MeV calculated with the G -matrix folding potentials. Solid, dashed, and dot-dashed curves are for MPa, MPb, and MPc, respectively. The dotted curve is for ESC.

MPa/b/c, respectively. Thus, the nuclear saturation property derived from MPa/b/c is quite reasonable in comparison with the empirical values.

The MPP parts in MPa and MPb are the same as MP1a and MP2a given in Ref. [10], respectively. The differences are in the TNA parts: Those of MPa and MPb are tuned so as to reproduce the saturation properties more accurately than those of MP1a and MP2a.

In Fig. 1, the calculated results of the differential cross sections for the $^{16}\text{O} + ^{16}\text{O}$ elastic scattering at $E/A = 70$ MeV are compared with the experimental data [18]. The corresponding $^{16}\text{O} + ^{16}\text{O}$ double-folding potentials are shown in Fig. 2. Here, the dotted curves are obtained from ESC, and the angular distribution deviates substantially from the data. Solid, dashed, and dot-dashed curves are for MPa, MPb, and MPc, respectively. These sets reproduce nicely the experimental data, though the fitting by MPc seems to be slightly worse than MPa/b. In this double-folding model analysis, most important is the validity of the frozen-density approximation (FDA): Owing to the FDA, the MPP repulsion in the density region over the normal density contributes to folding potentials. Such an effect can be seen in Fig. 2, where the potentials for MPa/b/c are remarkably shallower than that for ESC. Though reduction factors are often multiplied on the imaginary parts in the folding model analyses [9], such a reduction factor is not used in the present analysis. The necessity to include the quartic Pomeron coupling has to appear in the difference between results for MPa and MPb, but it cannot be found in the present analyses for nucleus-nucleus scattering.

Recently, a detailed analysis for the above $^{16}\text{O} + ^{16}\text{O}$ scattering was performed using the G -matrix double-folding potential derived from MPa with FDA [19]. Here, it has been investigated explicitly in regard to what densities MPPs contribute dominantly, and it was found that MPP contributions from the density region higher than the normal density are decisively important for resultant angular distributions. Thus,

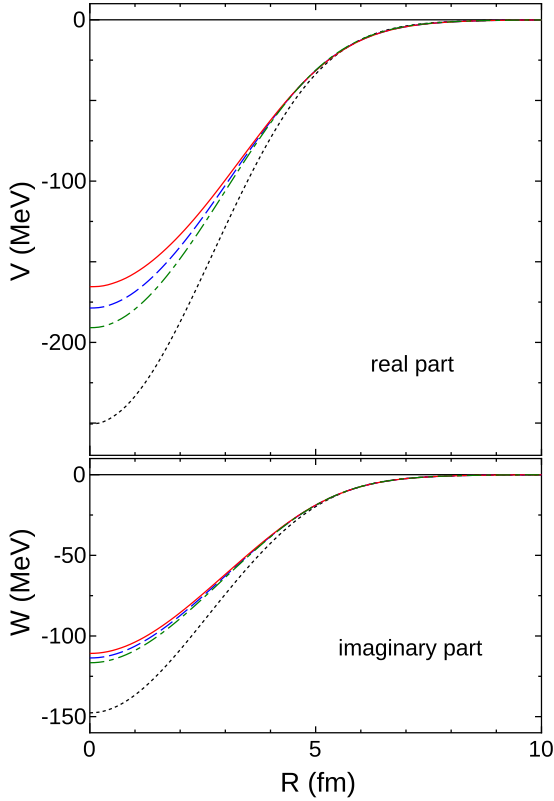


FIG. 2. (Color online) Double-folding potentials for $^{16}\text{O} + ^{16}\text{O}$ elastic scattering at $E/A = 70$ MeV. Solid, dashed, and dot-dashed curves are for MPa, MPb, and MPc, respectively. The dotted curve is for ESC.

we can say that valuable information of the EoS in high-density region can be obtained from double-folding potentials with FDA.

As given in [10], the mass-radius relations of neutron stars are obtained by solving the TOV equation with the neutron matter EoS. The maximum masses for MPa/b/c are $2.5M_{\odot}$, $2.2M_{\odot}$, and $2.1M_{\odot}$, respectively.

III. YN INTERACTION AND HYPERNUCLEI

Let us study here the properties of YN G -matrix interactions derived from ESC in symmetric nuclear matter including a single hyperon (Λ or Σ). Then, the correlations induced by baryonic coupling interactions such as ΛN - ΣN ones are renormalized into single-channel parts of G matrices. The hypernuclear phenomena and the underlying YN interaction models are linked through the models of hypernuclei and the YN G -matrix interactions, and then the hypernuclear information can be used to test the interaction models. Here, the G -matrix calculations are performed in the same way as in [20].

Here, the most important is to test the MPP + TBA parts in channels including hyperons. Though MPP is defined universally in all baryon channel, TBA is introduced phenomenologically in nucleon channels, and not defined in YN channels. Our strategy is to determine this part so as to be

TABLE II. Values of U_{Λ} at normal density and partial wave contributions in $^{2S+1}L_J$ states for ESC and MPa/b/c from the G -matrix calculations with CON prescriptions (in MeV). The value specified by D gives the sum of $^{2S+1}D_J$ contributions.

	1S_0	3S_1	1P_1	3P_0	3P_1	3P_2	D	U_{Λ}
ESC	-13.3	-26.7	2.6	0.2	1.8	-3.2	-1.6	-40.0
MPa	-13.6	-25.9	3.4	0.4	2.1	-1.7	-2.7	-38.1
MPb	-13.6	-26.0	3.4	0.4	2.1	-1.8	-2.7	-38.3
MPc	-13.4	-25.1	3.2	0.3	2.0	-2.1	-2.4	-37.4

consistent with hypernuclear data. As a trial, we assume it to be the same as for nucleon channels.

The ΛN G -matrix calculations are performed for ESC and MPa/b/c. In Table II we show the potential energies U_{Λ} for a zero-momentum Λ and their partial-wave contributions $U_{\Lambda}(^{2S+1}L_J)$ at normal density ρ_0 ($k_F = 1.35 \text{ fm}^{-1}$), where a statistical factor $(2J + 1)$ is included in $U_{\Lambda}(^{2S+1}L_J)$. As shown later, the Λ -nucleus folding potentials derived from these G matrices lead to Λ spectra consistent with hypernuclear data. As for the partial wave contributions, it is important that the odd-state contribution is weakly attractive. In the cases of NSC97e/f models, they are strongly repulsive [21]. Such a difference becomes remarkable in the high density region relevant to Λ mixing in neutron star matter. The Λ onset density is somewhat increased by strong odd-state repulsions [4]

For applications to finite systems, we derive k_F -dependent local potentials in coordinate space from the G matrices, and make Λ -nucleus folding potentials. In this procedure, densities $\rho(r)$ and mixed densities $\rho(r, r')$ of core nuclei are obtained from Skyrme Hartree-Fock wave functions. For the k_F -dependent parts of our localized G -matrix interactions, we use the averaged-density approximation: An averaged value $\langle k_F \rangle$ is calculated for each Λ state, and substituted into G matrices. The energy spectra of Λ hypernuclei ($^{13}_{\Lambda}\text{C}$, $^{28}_{\Lambda}\text{Si}$, $^{51}_{\Lambda}\text{V}$, $^{139}_{\Lambda}\text{La}$, $^{208}_{\Lambda}\text{Pb}$) are calculated with the G -matrix interactions obtained from MPa and ESC. In Fig. 3, the calculated values shown by solid (MPa) and dashed (ESC) lines are compared with the experimental values marked by open circles, where the horizontal axis is given as $A^{-2/3}$. Here, the experimental data are shifted by 0.5 MeV from the values given in Ref. [22], which has been recently proposed according to the improved calibration [23]. Our G -matrix folding models turn out to reproduce the energy spectra of Λ hypernuclei systematically with no free parameter in both cases of ESC and MPa. The results for MPb and MPc are very similar to that for MPa. It should be noted that reasonable Λ binding energies are obtained by taking the (MPP + TBA) parts equally to those in nucleon matter.

The similar results for MPa and ESC mean that the MPP and TBA contributions are somewhat canceled in evaluations of Λ binding energies. Here, the important point is that the results for (ESC + MPP + TBA) reproduce well the experimental values. This is considered a necessary condition which our MPP + TBA should satisfy in the normal density region.

When the results for MPa and ESC are compared carefully, we find some interesting differences. In Table III, the calculated values of the energy spectra of $^{89}_{\Lambda}\text{Y}$ for MPa and

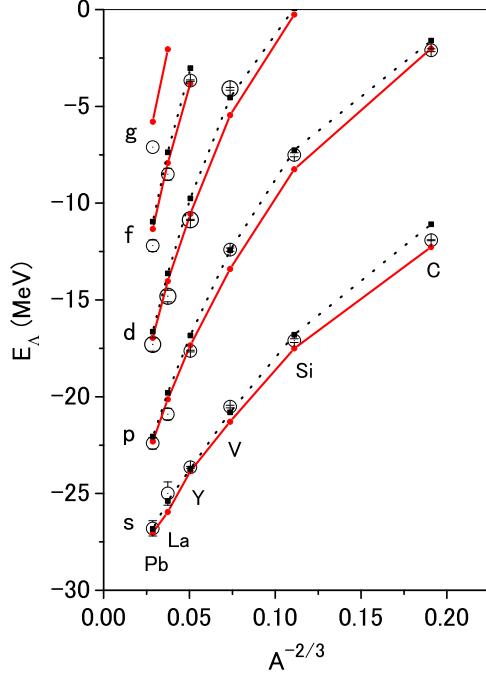


FIG. 3. (Color online) Energy spectra of Λ hypernuclei ($^{13}_{\Lambda}\text{C}$, $^{28}_{\Lambda}\text{Si}$, $^{51}_{\Lambda}\text{V}$, $^{139}_{\Lambda}\text{La}$, $^{208}_{\Lambda}\text{Pb}$) derived from MPA (solid lines) and ESC (dotted lines). Experimental values are marked by open circles.

ESC are compared with the experimental values. Values in parentheses are averaged values $\langle k_F \rangle$ which are evaluated self-consistently with solved Λ wave functions. The $^{89}_{\Lambda}\text{Y}$ data have been measured with high statistics and the obtained energy spectrum are very reliable. In this case the result for MPA is found to fit better than that for ESC. The reason is that the stronger density-dependent interaction of the former works more attractively in the upper states with smaller values of $\langle k_F \rangle$. As found in Fig. 3, the same effect brings about the larger binding energies in light systems such as $^{13}_{\Lambda}\text{C}$ with smaller values of $\langle k_F \rangle$, where the low-density contributions are dominant.

The stronger density dependence of MPA is due to the density-dependent contributions of the (MPP + TBA) part. It is expected that more systematical studies of Λ binding energies in future experiments will elucidate the strength of the density dependence more quantitatively.

TABLE III. Energy spectra (in MeV) of $^{89}_{\Lambda}\text{Y}$ calculated with MPA and ESC in comparison with experimental values. Averaged values of k_F (in fm^{-1}) are in parentheses.

	<i>s</i>	<i>p</i>	<i>d</i>	<i>f</i>
MPa	-23.8 (1.27)	-17.4 (1.23)	-10.6 (1.16)	-3.8 (1.08)
ESC	-23.7 (1.28)	-16.8 (1.23)	-9.8 (1.17)	-3.0 (1.09)
Expt.	-23.7	-17.6	-10.9	-3.7

IV. EOS AND NEUTRON STARS

A. Hyperonic nuclear matter

Let us derive here the EoS of baryonic matter composed of nucleons ($N = n, p$) and hyperons ($Y = \Lambda, \Sigma^-$) on the basis of the Brueckner theory.

We start from baryon single particle potentials. From G -matrix elements in momentum space, a single-particle potential of a B particle in B' matter is given by

$$U_B(k) = \sum_{B'} U_B^{(B')}(k) = \sum_{B'} \sum_{k', k_F^{(B')}} \langle kk' | G_{BB', B'B'} | kk' \rangle \quad (5)$$

with $B, B' = N, Y$. Here, spin-isospin quantum numbers are implicit. The energy density is given by

$$\begin{aligned} \varepsilon &= \varepsilon_{\text{kin}} + \varepsilon_{\text{pot}} \\ &= 2 \sum_B \int_0^{k_F^B} \frac{d^3k}{(2\pi)^3} \left\{ \frac{\hbar^2 k^2}{2M_B} + \frac{1}{2} U_B(k) \right\}. \end{aligned} \quad (6)$$

Then, we have

$$\int_0^{k_F^B} \frac{k^2 dk}{\pi^2} U_B^{(B')}(k) = \int_0^{k_F^{B'}} \frac{k^2 dk}{\pi^2} U_{B'}^{(B)}(k).$$

Considering $\rho_B = \frac{(k_F^B)^3}{3\pi^2}$,

$$\frac{\partial}{\partial \rho_B} \mathcal{U}_B^{(B')} = U_B^{(B')}(k_F^B) + \int_0^{k_F^B} \frac{k^2 dk}{\pi^2} \frac{\partial U_B^{(B')}(k)}{\partial \rho_B} \quad (7)$$

The second term leads to the rearrangement contribution.

The baryon number density is given as $\rho = \sum_B \rho_B$, ρ_B being the density for component B . Then, the chemical potentials μ_B and pressure P are expressed as

$$\mu_B = \frac{\partial \varepsilon}{\partial \rho_B}, \quad (8)$$

$$P = \rho^2 \frac{\partial(\varepsilon/\rho)}{\partial \rho_B} = \sum_B \mu_B \rho_B - \varepsilon. \quad (9)$$

In Figs. 4 and 5, $U_{\Lambda}^{(n)}$ for $\rho_{\Lambda}/\rho_n = 0.2$ and $U_{\Sigma^-}^{(n)}$ for $\rho_{\Sigma^-}/\rho_n = 0.2$ are drawn as functions of ρ_n , respectively. Here, solid, dashed, dot-dashed, and dotted curves are for MPA, MPb, MPc, and ESC, respectively. In the cases of MPA/b/c, we find the large repulsive contributions from their MPP parts. The solid curves (MPa) are steeper than the dashed (MPb) and dot-dashed (MPc) curves due to the four-body repulsion included in MPA. The values of $U_{\Sigma^-}^{(n)}$ should be noted to be substantially repulsive even for ESC without MPP contributions. The $n\Sigma^-$ interactions are dominated by contributions in 3S_1 $T = 3/2$ states. The strongly repulsive contribution in this state is due to the Pauli-forbidden state effect taken into account by strengthening the Pomeron coupling in the ESC modeling [6].

We introduce some approximations to calculate the energy density of baryonic matter: (1) Hyperonic energy densities including Λ and Σ^- are obtained from calculations of $n + p + \Lambda$ and $n + p + \Sigma^-$ systems, respectively. (2) The parabolic approximation is used to treat asymmetries between n and p

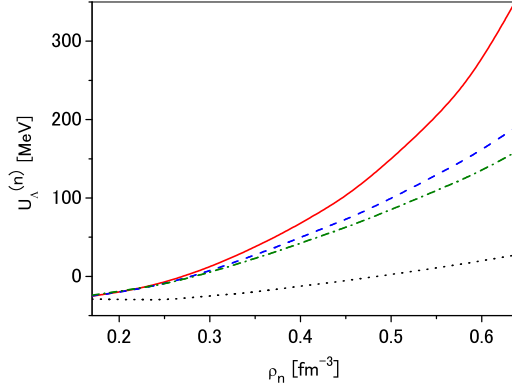


FIG. 4. (Color online) $U_\Lambda^{(n)}$ for $\rho_\Lambda/\rho_n = 0.2$ as a function of ρ_n . Solid, dashed, dot-dashed, and dotted curves are for MPa, MPb, MPc, and ESC, respectively.

in $n + p$ sectors. The calculated values of energy densities are fitted by the following analytical parametrization [24]:

$$\varepsilon_{\text{pot}}(\rho_n, \rho_p, \rho_\Lambda, \rho_\Sigma) = E_N \rho_N + (E_\Lambda + E_{\Lambda\Lambda})\rho_\Lambda + (E_\Sigma + E_{\Sigma\Sigma})\rho_\Sigma. \quad (10)$$

$$E_z = (1 - \beta)f_z^{(0)} + \beta f_z^{(1)} \quad (11)$$

with $z = N, \Lambda, \Sigma, \Lambda\Lambda, \Sigma\Sigma$. Here, we have $\beta = (1 - 2x_p)^2$ with $x_p = \rho_p/\rho_N$ and $\rho_N = \rho_n + \rho_p$. Expressions of $f_z^{(i)}$ with $i = 0, 1$ are given as

$$f_N^{(i)} = a_N^{(i)}\rho_N + b_N^{(i)}\rho_N^{c_N^{(i)}}, \quad (12)$$

$$f_y^{(i)} = A_y^{(i)}\rho_N + B_y^{(i)}\rho_N^{c_Y^{(i)}}, \quad (13)$$

$$A_y^{(i)} = a_{y0}^{(i)} + a_{y1}^{(i)}x_Y + a_{y2}^{(i)}x_Y^2, \quad (14)$$

$$B_y^{(i)} = b_{y0}^{(i)} + b_{y1}^{(i)}x_Y + b_{y2}^{(i)}x_Y^2, \quad (15)$$

where $x_Y = \rho_Y/\rho_N$ with $Y = \Lambda, \Sigma$, and $y = \Lambda, \Sigma, \Lambda\Lambda, \Sigma\Sigma$. In the above expressions, N, Λ , and Σ ($\Lambda\Lambda$ and $\Sigma\Sigma$) denote contributions from $NN, N\Lambda$, and $N\Sigma^-$ ($\Lambda\Lambda$ and $\Sigma^-\Sigma^-$) interactions, respectively.

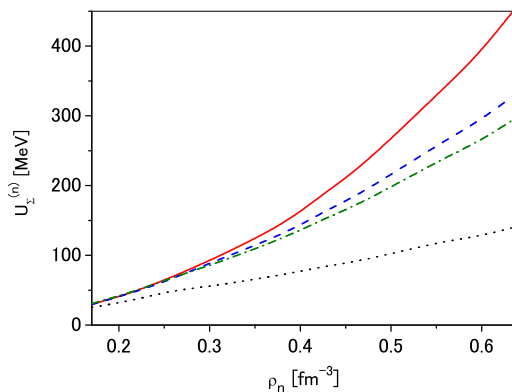


FIG. 5. (Color online) $U_\Sigma^{(n)}$ for $\rho_\Sigma/\rho_n = 0.2$ as a function of ρ_n . Also see the caption of Fig. 4.

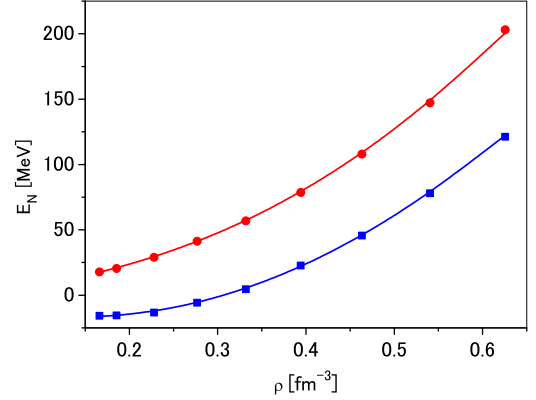


FIG. 6. (Color online) Square and circle marks are calculated values of E_N with MPa for symmetric and neutron matter, respectively. Fitting functions are shown by solid curves.

Now, the G -matrix calculations with the CON choice are performed with ESC and MPa/b/c sets in the density region of $\rho_0 < \rho_B < 4\rho_0$, and the results are fitted in the above functional forms. Our fitting procedures are as follows: First, values of E_N in symmetric nucleon matter and neutron matter are calculated for various values $\rho_N = 0.17\text{--}0.7 \text{ fm}^{-3}$, and fitted by a function $a\rho_N + b\rho_N^c$ with parameters a, b , and c . In Fig. 6, calculated values of E_N for MPa are shown by square and circle marks for symmetric and neutron matter, respectively. The corresponding fitting functions are shown by solid curves, where the quality of fitting is found to be quite nice. Next, values of E_Λ are calculated in neutron matter and symmetric nucleon matter including Λ . They are obtained for $\rho_N = 0.17\text{--}0.7 \text{ fm}^{-3}$ and $x_\Lambda = 0.1, 0.2, 0.3$. In Fig. 7, calculated values of E_Λ for MPa in the $n + \Lambda$ case are shown by square, circle, and triangle marks for $x_\Lambda = 0.1, 0.2, 0.3$, respectively. The corresponding fitting functions with $a\rho_N + b\rho_N^c$ forms are shown by solid curves, where a common value of c is taken for the three cases. Then, values of a and b for $x_\Lambda = 0.1, 0.2, 0.3$ are fitted by a quadratic function of x_Λ . A similar figure and parameters are obtained in the case of symmetric matter including Λ . The same fitting procedures

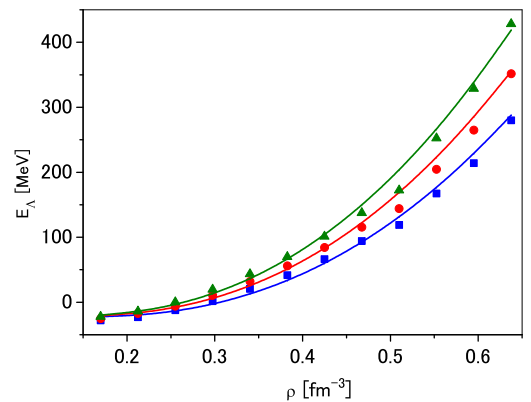


FIG. 7. (Color online) Calculated values of E_Λ with MPa in the $n + \Lambda$ case. Square, circle, and triangle marks are for $x_\Lambda = 0.1, 0.2, 0.3$, respectively. Fitting functions are shown by solid curves.

TABLE IV. Parameters of energy densities for MPa given by analytical forms Eqs. (10)–(15).

$a_N^{(0)}$	$b_N^{(0)}$	$c_N^{(0)}$		$a_N^{(1)}$	$b_N^{(1)}$	$c_N^{(1)}$
-234.8	643.8	1.86		66.41	490.1	2.40
$a_{\Lambda 0}^{(0)}$	$a_{\Lambda 1}^{(0)}$	$a_{\Lambda 2}^{(0)}$	$b_{\Lambda 0}^{(0)}$	$b_{\Lambda 1}^{(0)}$	$b_{\Lambda 2}^{(0)}$	$c_{\Lambda}^{(0)}$
-436.4	1198.	-2790.	1648.	-3970.	12730.	2.29
$a_{\Lambda 0}^{(1)}$	$a_{\Lambda 1}^{(1)}$	$a_{\Lambda 2}^{(1)}$	$b_{\Lambda 0}^{(1)}$	$b_{\Lambda 1}^{(1)}$	$b_{\Lambda 2}^{(1)}$	$c_{\Lambda}^{(1)}$
-215.2	14.17	-202.7	1117.	2283.	-198.5	2.56
$a_{\Sigma 0}^{(0)}$	$a_{\Sigma 1}^{(0)}$	$a_{\Sigma 2}^{(0)}$	$b_{\Sigma 0}^{(0)}$	$b_{\Sigma 1}^{(0)}$	$b_{\Sigma 2}^{(0)}$	$c_{\Sigma}^{(0)}$
-5.017	-618.6	1444.	382.1	1803.	-2748.	2.00
$a_{\Sigma 0}^{(1)}$	$a_{\Sigma 1}^{(1)}$	$a_{\Sigma 2}^{(1)}$	$b_{\Sigma 0}^{(1)}$	$b_{\Sigma 1}^{(1)}$	$b_{\Sigma 2}^{(1)}$	$c_{\Sigma}^{(1)}$
100.4	178.5	-186.2	909.9	1875.	-1071.	2.65
$a_{\Lambda\Lambda 0}^{(1)}$	$a_{\Lambda\Lambda 1}^{(1)}$	$a_{\Lambda\Lambda 2}^{(1)}$	$b_{\Lambda\Lambda 0}^{(1)}$	$b_{\Lambda\Lambda 1}^{(1)}$	$b_{\Lambda\Lambda 2}^{(1)}$	$c_{\Lambda\Lambda}^{(1)}$
.7345	-92.92	57.59	-4.144	419.9	480.7	2.27

are performed for E_{Σ} and $E_{\Lambda\Lambda}$. Generally, the quality of fitting for E_y in hyperonic matter is inferior to that for E_N in nucleon matter. The values of fitted parameters for MPa are listed in Table IV. Here, $\Lambda\Lambda$ ($i = 0$) parts are omitted in the table, because their effects are negligible in the following results. $\Sigma^-\Sigma^-$ and $\Lambda\Sigma^-$ interactions are not taken into account in the present work.

As discussed later, the EoS's for MPa violate causality and predict sound speeds over the speed of light above a critical density. Then, we adopt the approximation where the EoS is replaced by the causal EoS above this density in the same way as the treatment in [25].

B. EoS of hyperon-mixed neutron-star matter

Our neutron-star matter is composed of n , p , e^- , μ^- , Λ , and Σ^- . The equilibrium conditions are summarized as follows:

(1) chemical equilibrium conditions,

$$\mu_n = \mu_p + \mu_e, \quad (16)$$

$$\mu_{\mu} = \mu_e, \quad (17)$$

$$\mu_{\Lambda} = \mu_n, \quad (18)$$

$$\mu_{\Sigma^-} = \mu_n + \mu_e; \quad (19)$$

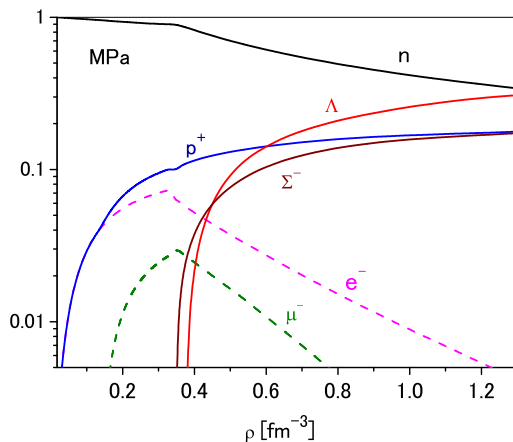


FIG. 8. (Color online) Composition of hyperonic neutron-star matter in the case of MPa.

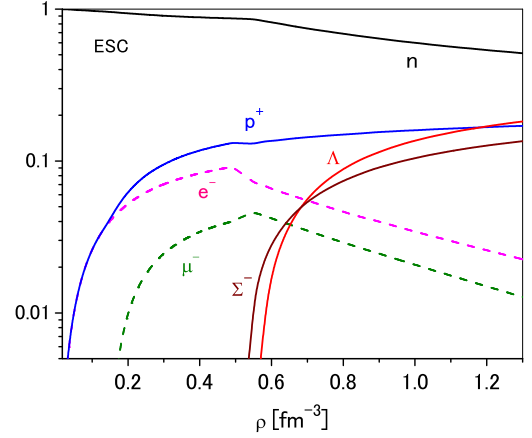


FIG. 9. (Color online) Composition of hyperonic neutron-star matter in the case of ESC.

(2) charge neutrality,

$$\rho_p = \rho_e + \rho_{\mu} + \rho_{\Sigma^-}; \quad (20)$$

(3) baryon number conservation,

$$\rho = \rho_n + \rho_p + \rho_{\Lambda} + \rho_{\Sigma^-}. \quad (21)$$

When the analytical expressions (10)–(15) are substituted into the chemical potentials (8), the chemical equilibrium conditions (16)–(19) are represented as equations for densities ρ_a ($a = n, p, e^-, \mu^-, \Lambda$, and Σ^-). Then, Eqs. (16)–(21) can be solved iteratively.

In Figs. 8 and 9, the matter compositions are shown in the cases of MPa and ESC, respectively. Comparing the two figures, we note some effects of MPP contributions: (1) The onset densities of hyperon mixing for MPa are lower than those for ESC. (2) Hyperon components for MPa are larger than those for ESC. (3) Larger hyperon components for MPa are covered by smaller components of n , e^- , and μ^- , and proton components are not so different from each other. In Table V, the onset densities of hyperon mixing are given for MPa/b/c and ESC. Thus, increasing MPP repulsions are found to enhance hyperon mixings.

Here, let us see the role of MPP repulsions in more detail. The repulsions among neutrons make single-particle potentials shallower, which allows easier conversions of neutrons into hyperons. These effects are partially canceled out by the repulsions including hyperons, which make shallower hyperon single-particle potentials. As seen in Table V, for instance, the onset densities of Σ^- and Λ are 0.52 and 0.54 fm^{-3} for ESC, respectively. If only the (MPP + TBA) contributions among nucleons are taken into account in the case of MPa, both of

 TABLE V. Onset densities in fm^{-3} .

Model	Σ^-	Λ
MPa	0.34	0.36
MPb	0.37	0.42
MPc	0.39	0.45
ESC	0.52	0.54

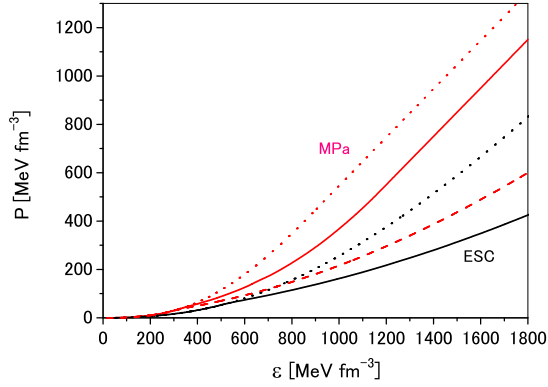


FIG. 10. (Color online) Pressure P as a function of energy density ε in the cases of MPA (upper curves) and ESC (lower curves). Solid and dotted curves are with and without hyperon mixing, respectively. In the dashed curve with hyperon mixing, MPP + TBA parts are switched off in channels including hyperons.

them are 0.32 fm^{-3} . Then, the values of 0.34 and 0.36 fm^{-3} for MPA are understood as a result of partial canceling of the MPP repulsive effects.

Pressures (11) are derived from determined values of densities and chemical potentials. In Figs. 10 and 11, the calculated values of pressure P are drawn as functions of energy density ε and baryon density ρ , respectively, in the cases of MPA (upper curves) and ESC (lower curves). Here, solid and dotted curves are with and without hyperon mixing, respectively. The dashed curve is with hyperon mixing, where the MPP + TBA parts are included only in nucleon channels. The differences between the two dotted curves are due to the MPP repulsive contributions among nucleons, and the remarkable softening from the upper dotted curve to the dashed curve is brought about by hyperon mixing. This softening is substantially recovered when the MPP contributions are included universally among baryons.

C. Neutron stars

Using the EoS of hyperonic neutron matter, we solve the TOV equation for the hydrostatic structure of a spherical

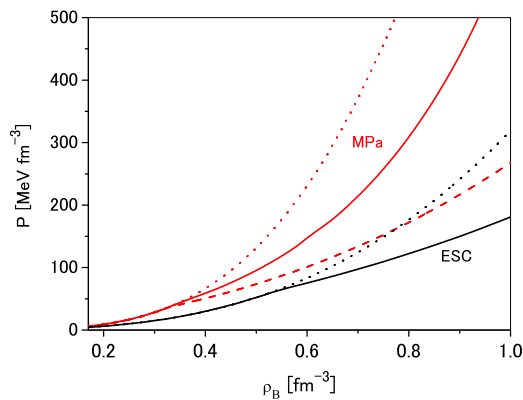


FIG. 11. (Color online) Pressure P as a function of baryon density ρ_B in the cases of MPA (upper curves) and ESC (lower curves). Also see the caption of Fig. 10.

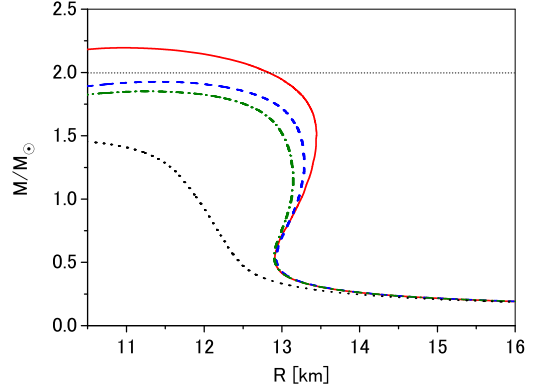


FIG. 12. (Color online) Neutron-star masses as a function of the radius R . Solid, dashed, dot-dashed, and dotted curves are for MPA/b/c and ESC, respectively.

nonrotating star, and obtain the masses and radii of neutron stars. The EoS's for MPA/b/c and ESC are used for $\rho > \rho_0$. Below ρ_0 we use the EoS of the crust obtained in [26,27]. Then, the EoS's for $\rho > \rho_0$ and $\rho < \rho_0$ are connected smoothly.

In Fig. 12, neutron-star masses are drawn as a function of radius, where solid, dashed, dot-dashed, and dotted curves are for MPA/b/c and ESC, respectively. Then, calculated values of maximum masses M/M_\odot are $2.20M_\odot$, $1.93M_\odot$, and $1.85M_\odot$ for MPA/b/c, respectively. These values are smaller by about $0.3M_\odot$ than the values without hyperon mixing. Thus, the maximum mass only for MPA is noted to be substantially larger than the observed value of $\sim 2M_\odot$ owing its four-body repulsive contribution. It should be noted that the difference between MPA and MPc comes from the four-body repulsion included in the former, because MPc is made by switching off the four-body part from MPA. On the other hand, MPb is designed so as to reproduce the repulsive effect of MPA in the ^{16}O - ^{16}O scattering without the four-body repulsive part. The difference between MPA and MPb originates from the steeper EoS of MPA by the four-body repulsion in the high-density region.

The mass-radius relations in Fig. 13 demonstrate the effects of hyperon mixings and MPP contributions. Here, dotted and

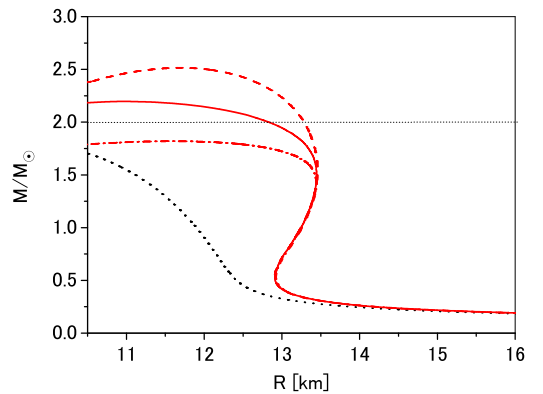


FIG. 13. (Color online) Neutron-star masses as a function of the radius R . Dashed and dotted curves are obtained from MPA and ESC, respectively, without hyperon mixing. The solid (dot-dashed) curve is obtained with hyperon mixing, where MPP contributions are included in all baryons universally (only in nucleon sectors).

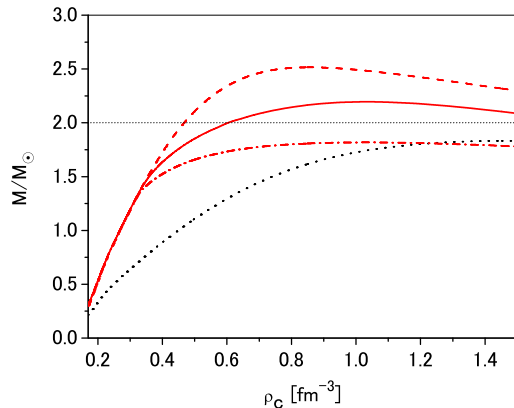


FIG. 14. (Color online) Neutron-star masses as a function of the central density ρ_c . Also see the caption of Fig. 13.

dashed curves are obtained from ESC and MPa, respectively, without hyperon mixing. Then, the remarkable differences between dotted and dashed curves are due to the MPP contributions among nucleons included in MPa. Solid and dot-dashed curves are obtained with hyperon mixing. Here, the MPP contributions in the former (latter) are included in all baryons universally (only in nucleon sectors). When the MPP contributions are included only in nucleon sectors, the maximum mass in the dashed curve with $2.51M_\odot$ is strongly reduced to $1.82M_\odot$ in the dot-dashed one by the effect of hyperon mixing. When the MPP contributions are taken into account universally in all baryons, the maximum mass is recovered to $2.20M_\odot$ in the solid curve. We can find the same demonstration in Fig. 14 where the corresponding curves of neutron-star masses are drawn as a function of central density ρ_c .

In our calculations, the causality conditions at very high density are violated in the case of using MPa, and not in MPb and MPC cases. The critical density for MPa, sound speeds being over the speed of light, is obtained as 0.97 (0.74) fm^{-3} in the case of (not) including hyperon mixing. As found in Fig. 14, the masses M/M_\odot take the maximum values at ~ 1.0 (~ 0.85) fm^{-3} in the case of (not) including hyperon mixing. Our criterion for the violation of the causality condition is whether or not the critical density is above the density giving the maximum mass. Thus, we can say that the hyperon-mixed result with MPa is almost free from the violation of the causality condition. On the other hand, it is violated significantly in the corresponding result without hyperon mixing.

Recently, neutron stars with $2M_\odot$ have been studied with use of hyperon-mixed EoS's based on the relativistic mean-field (RMF) approximation [28]. They have found that basic features of our EoS for MPa are similar to those of their successful RMF models.

V. CONCLUSION

The existence of neutron stars with $2M_\odot$ gives a severe condition for the stiffness of the EoS of neutron-star matter, namely the necessity of the strong TNR. On the other hand,

hyperon mixing in neutron-star matter brings about a remarkable softening of the EoS, which cancels the TNR effect for the maximum mass. As a possibility to avoid this serious problem, we introduce the TNR-like repulsions working universally for YNN , YYN , YYY , as well as for NNN [5].

On the basis of the BB interaction model ESC, we introduce the universal three-body repulsion MPP among three baryons. The strengths of MPP are determined by fitting the observed angular distribution of $^{16}\text{O} + ^{16}\text{O}$ elastic scattering at $E_{in}/A = 70$ MeV with use of the G -matrix folding potential. Then, TNA is added to MPP phenomenologically so as to reproduce the minimum value ~ -16 MeV of the energy per nucleon at normal density 0.16 fm^{-3} in symmetric nuclear matter as well as the $^{16}\text{O} + ^{16}\text{O}$ data. In this modeling, the empirical values of K , E_{sym} , and L are reproduced reasonably. The EoS of neutron-star matter obtained from ESC + MPP + TNA is stiff enough to give the large neutron-star mass over $2M_\odot$, when the hyperon mixing is not taken into account.

In order to study the effect of hyperon mixing on the EoS and mass-radius relations of neutron stars, we need to use reliable interactions in channels including hyperons. The reliability of ESC in these channels has been confirmed by successful applications to hypernuclear systems. Our MPP contributions exist universally in every baryonic system. Assuming that the remaining part TNA also contributes universally as TBA, ESC + MPP + TBA can be tested in applications to hypernuclei: The energy spectra of Λ hypernuclei are nicely reproduced by the derived G matrix interactions with no modification for TBA. Then, it is suggested that inclusion of MPP + TBA leads to even better fitting than the case of using ESC part only.

The EoS of hyperonic nuclear matter is obtained from ESC + MPP + TBA on the basis of the G -matrix approach, and the mass-radius relations of neutron stars are derived by solving the TOV equation. In spite of remarkable softening of EoS caused by hyperon mixing, its substantial part is recovered owing to the MPP contributions. As a result, the universal MPP repulsions are shown to bring about hyperon-mixed neutron stars with masses $\sim 2M_\odot$. It should be noted that our conclusion for neutron stars is obtained essentially on the basis of terrestrial experiments without using *ad hoc* parameters to stiffen the EoS. However, there still remains some ambiguity demonstrated in the difference between the mass-radius relations for MPa and MPb, both of which reproduce almost the same results in our analysis for $^{16}\text{O} + ^{16}\text{O}$ elastic scattering. The difference between MPa and MPb originates from the four-body repulsion included in the former. It is an interesting subject to confirm its existence clearly in terrestrial experiments.

While we did not take into account the existence of quarks in this study, it should be considered. The quark-hadron phase transition is, however, beyond the scope of the baryonic approach in the present work; it strongly depends on quark models, and the transition itself has high uncertainty. Actually, no one knows whether the transition is first order [29] or crossover [30]. Even if we assume that the phase transition is first order, there is the uncertainty caused by the finite-size effect [31]. It is our work in the near future to consider the quark-hadron phase transition.

- [1] P. B. Demorest, T. Pennucci, S. M. Ransom, M. S. E. Roberts, and J. W. Hessels, *Nature (London)* **467**, 1081 (2010).
- [2] J. Antoniadis *et al.*, *Science* **340**, 6131 (2013).
- [3] M. Baldo, G. F. Burgio, and H.-J. Schulze, *Phys. Rev. C* **61**, 055801 (2000).
- [4] I. Vidana, A. Polls, A. Ramos, L. Engvik, and M. Hjorth-Jensen, *Phys. Rev. C* **62**, 035801 (2000).
- [5] S. Nishizaki, Y. Yamamoto, and T. Takatsuka, *Prog. Theor. Phys.* **105**, 607 (2001); **108**, 703 (2002).
- [6] Th. A. Rijken, M. M. Nagels, and Y. Yamamoto, *Prog. Theor. Phys. Suppl.* **185**, 14 (2010).
- [7] Th. A. Rijken, M. M. Nagels, and Y. Yamamoto, *Genshikaku Kenkyu* **57** (Suppl. 3), 6 (2013).
- [8] M. Baldo, A. Fiasconaro, H. Q. Song, G. Giansiracusa, and U. Lombardo, *Phys. Rev. C* **65**, 017303 (2001).
- [9] T. Furumoto, Y. Sakuragi, and Y. Yamamoto, *Phys. Rev. C* **79**, 011601(R) (2009); **80**, 044614 (2009).
- [10] Y. Yamamoto, T. Furumoto, N. Yasutake, and Th. A. Rijken, *Phys. Rev. C* **88**, 022801(R) (2013).
- [11] S. Weissenborn, D. Chatterjee, and J. Schaffner-Bielich, *Nucl. Phys. A* **881**, 62 (2012).
- [12] I. Bednarek, P. Haensel, J. L. Zdunik, M. Bejger, and R. Mańka, *Astron. Astrophys.* **543**, A157 (2012).
- [13] W.-Z. Jiang, B.-A. Li, and L.-W. Chen, *Astrophys. J.* **756**, 56 (2012).
- [14] A. B. Kaidalov and K. A. Ter-Matrosyan, *Nucl. Phys.* **74**, 471 (1974).
- [15] J. B. Bronzan and R. L. Sugar, *Phys. Rev. D* **16**, 466 (1977).
- [16] I. E. Lagaris and V. R. Pandharipande, *Nucl. Phys. A* **359**, 349 (1981).
- [17] P. Möller, W. D. Myers, H. Sagawa, and S. Yoshida, *Phys. Rev. Lett.* **108**, 052501 (2012).
- [18] F. Nuoffer *et al.*, *Nuovo Cimento A* **111**, 971 (1998).
- [19] T. Furumoto, Y. Sakuragi, and Y. Yamamoto, *Phys. Rev. C* **90**, 041601(R) (2014).
- [20] Y. Yamamoto, T. Motoba, and Th. A. Rijken, *Prog. Theor. Phys. Suppl.* **185**, 72 (2010).
- [21] Th. A. Rijken, V. G. J. Stoks, and Y. Yamamoto, *Phys. Rev. C* **59**, 21 (1999).
- [22] O. Hashimoto and H. Tamura, *Prog. Part. Nucl. Phys.* **57**, 564 (2006).
- [23] T. Gogami, Doctor thesis, Tohoku University, 2014 (unpublished).
- [24] N. Yasutake, G. F. Burgio, and H.-J. Schulze, *Phys. At. Nuclei* **74**, 1502 (2011).
- [25] S. Gandolfi, J. Carlson, and Sanjjay Reddy, *Phys. Rev. C* **85**, 032801(R) (2012).
- [26] G. Baym, A. Bethe, and C. Pethick, *Nucl. Phys. A* **175**, 225 (1971).
- [27] G. Baym, C. J. Pethick, and P. Sutherland, *Astrophys. J.* **170**, 299 (1971).
- [28] M. Fortin, J. L. Zdunik, P. Haensel, and M. Bejger, *arXiv:1408.3052*.
- [29] N. Yasutake, R. Łastowiecki, S. Benić, D. Blaschke, T. Maruyama, and T. Tatsumi, *Phys. Rev. C* **89**, 065803 (2014), and the references therein.
- [30] K. Masuda, T. Hatsuda, and T. Takatsuka, *Astrophys. J.* **764**, 12 (2013).
- [31] N. Yasutake, T. Noda, H. Sotani, T. Maruyama, and T. Tatsumi, *Recent Advances in Quarks Research* (Nova Science, Hauppauge, NY, 2013), Chap. 4, p. 63.